RESEARCH ARTICLE

Key Points:
- A thorough assessment of the seepage face boundary condition for subsurface and integrated hydrological models is performed
- A generalized algorithm is presented that handles heterogeneity in a simple way and establishes a link with atmospheric boundary conditions
- In the context of groundwater/surface water modeling, seepage face and outlet boundaries can coexist and both play important roles

Correspondence to:
C. Scudeler,
carlotta.scudeler@gmail.com

Examination of the seepage face boundary condition in subsurface and coupled surface/subsurface hydrological models

C. Scudeler[1,2,3] (iD), C. Paniconi[1] (iD), D. Pasetto[4] (iD), and M. Putti[2]

[1]Institut National de la Recherche Scientifique, Centre Eau Terre Environnement, Université du Québec, Quebec City, Canada, [2]Department of Mathematics, University of Padova, Padova, Italy, [3]Risk Management Solutions, Model Development, London, United Kingdom, [4]Laboratory of Ecohydrology, École Polytechnique Fédérale de Lausanne, Lausanne, Switzerland

Abstract A seepage face is a nonlinear dynamic boundary that strongly affects pressure head distributions, water table fluctuations, and flow patterns. Its handling in hydrological models, especially under complex conditions such as heterogeneity and coupled surface/subsurface flow, has not been extensively studied. In this paper, we compare the treatment of the seepage face as a static (Dirichlet) versus dynamic boundary condition, we assess its resolution under conditions of layered heterogeneity, we examine its interaction with a catchment outlet boundary, and we investigate the effects of surface/subsurface exchanges on seepage faces forming at the land surface. The analyses are carried out with an integrated catchment hydrological model. Numerical simulations are performed for a synthetic rectangular sloping aquifer and for an experimental hillslope from the Landscape Evolution Observatory. The results show that the static boundary condition is not always an adequate stand-in for a dynamic seepage face boundary condition, especially under conditions of high rainfall, steep slope, or heterogeneity; that hillslopes with layered heterogeneity give rise to multiple seepage faces that can be highly dynamic; that seepage face and outlet boundaries can coexist in an integrated hydrological model and both play an important role; and that seepage faces at the land surface are not always controlled by subsurface flow. The paper also presents a generalized algorithm for resolving seepage face outflow that handles heterogeneity in a simple way, is applicable to unstructured grids, and is shown experimentally to be equivalent to the treatment of atmospheric boundary conditions in subsurface flow models.

1. Introduction

A seepage face is the boundary between a saturated flow field and the atmosphere, or between a saturated flow field and a stream channel, where water is free to exit from the subsurface. The study of seepage faces is a central component of many geotechnical, hydrogeological, and geomorphological studies. In geotechnical engineering, seepage analysis is of interest for the design of hydraulic structures such as earth dams or river embankments [*Hirschfeld and Poulos*, 1973; *Milligan*, 2003] and in slope stability analysis [*Rulon and Freeze*, 1985; *Crosta and Prisco*, 1999; *Lee et al.*, 2008; *Orlandini et al.*, 2015]. In hydrogeology, seepage faces play a central role in the interactions between surface water and groundwater [*Sophocleous*, 2002], enhancing, for example, the flow to a stream channel within the time frame of a storm hydrograph [*Beven*, 1989], and in contamination migration and attenuation, controlling flow paths in the riparian zone [*Hill*, 1990] and the spreading of solutes in tailing impoundments [*Heikkinen et al.*, 2009; *Ferguson et al.*, 2009].

Early analyses of groundwater flow in the presence of a seepage face involved flow net techniques [*Casagrande*, 1937]. This approach is valid if the soil is homogeneous and saturated, the boundaries well defined, and the system at steady state, conditions that are rarely encountered in reality. Numerical models provide a more flexible and accurate approach to solving groundwater flow and seepage problems. Early subsurface hydrological models were limited to solving the saturated flow equation or various simplifications of this equation (e.g., Boussinesq models) based on, for example, hydraulic groundwater theory [*Troch et al.*, 2013]. In saturated flow and Boussinesq models, the seepage boundary that regulates groundwater drainage is often treated as a fixed Dirichlet condition, with atmospheric pressure assigned to the designated outflow nodes. This is a static, and therefore approximate, treatment of this dynamic boundary. Alternatively, in

saturated flow models based on the free surface approach, the position of the phreatic surface, and thus of the exit point along the seepage boundary, can evolve over time [e.g., *Isaacs*, 1980; *Shamsai and Narasimhan*, 1991].

Advances in numerical techniques together with the increased performance of high-speed digital simulation computers have led to numerical models based on Richards' equation for flow in variably saturated porous media becoming a widely used current approach for representing and solving seepage face problems. *Freeze* [1971] presented one of the first three-dimensional (3-D) finite difference models for transient saturated-unsaturated groundwater flow and used it for the study of heterogeneous anisotropic aquifers in the presence of a seepage face boundary. In the early finite element variably saturated flow models of *Rubin* [1968], *Neuman et al.* [1975], and *Cooley* [1983], an algorithm for locating the exit point of the seepage face at each iteration of the nonlinear system solver was incorporated into the overall numerical procedure. The localization scheme positions the exit point such that all nodes below it are at atmospheric pressure (a Dirichlet condition), allowing outflow to occur, while all nodes above it are assigned a no-flow (Neumann) condition, so that the nodes take on negative pressures (atmospheric pressure is the zero datum). The presence of a surface water body (hydrostatic Dirichlet nodes below the exit point) can also be incorporated [*Tracy and Mariño*, 1987]. The seepage face is thus treated as a combination of Dirichlet and Neumann boundary conditions that evolves in time and space, with the exit point rising during rainfall events, for example, and falling during recession periods.

Numerical models are essential for resolving flow dynamics in the presence of soil heterogeneity. Spatial variability of hydraulic properties may lead to complex interactions between the saturated and unsaturated zones, formation of perched water tables, and multiple seepage faces and exit points, which are impossible to model with graphical or analytical approaches. *Eigenbrod and Morgenstern* [1972] investigated a layered slope located in a river valley near Edmonton, Alberta, and their analysis revealed the presence of two perched water tables. A study performed by *Sterrett and Edil* [1982] shows how a complex flow system with double seepage faces formed at the land-lake interface along the shoreline of Lake Michigan (Wisconsin) due to inhomogeneities of the glacial materials. *Cooley* [1983] was the first to model drainage involving double seepage faces, for a case involving two soil layers separated by an impeding layer. A similar soil configuration was considered by *Rulon et al.* [1985] for their laboratory sand-tank experiments. In a steady state flow analysis using the finite element model of *Neuman* [1973] modified to account for a double seepage face, *Rulon et al.* [1985] showed that the response of the exit points is strongly dependent on the position of the impeding layer. Subsequently, *Lam et al.* [1987] simulated the same experiment considering transient conditions and infiltration.

The current generation of detailed physically based models that couple surface and subsurface flow were first introduced almost 20 years ago [*Bixio et al.*, 1999; *VanderKwaak*, 1999] but still require careful assessment of various implementation details, including the consistency and interactions between the outflow boundary conditions of each component model [*Paniconi and Putti*, 2015]. Examples of models that represent surface and subsurface systems as a continuum and are capable of simulating complex scenarios at different spatial and temporal scales include: ATS [*Painter et al.*, 2013; *Coon et al.*, 2016], CATHY [*Bixio et al.*, 1999; *Camporese et al.*, 2010], HydroGeoSphere [*Sudicky et al.*, 2008; *Therrien et al.*, 2012], InHM [*VanderKwaak*, 1999; *VanderKwaak and Loague*, 2001], OpenGeoSys [*Kolditz et al.*, 2012; *Delfs et al.*, 2012], and ParFlow [*Kollet and Maxwell*, 2006, 2008]. Recent intercomparison studies have shown that integrated models that impose continuity of both pressure head and water flux at the land surface produce similar responses [*Sulis et al.*, 2010; *Maxwell et al.*, 2014; *Kollet et al.*, 2016]. This continuity condition can be guaranteed with or without the introduction of an additional parameter, and the surface and subsurface equations can be solved in either a fully coupled mode or with a time-splitting technique in sequential iteration mode, this last approach being well-established in multiphysics simulations for coupling a wide diversity of phenomena [*Keyes et al.*, 2013].

Intriguing scenarios can arise when a catchment outlet condition (surface routing model) and a seepage face (subsurface model) coexist, the former inducing convergent flow patterns toward the land surface while the latter drives flow toward the base of the hillslope. This was seen recently during the first experiment performed on one of the artificial hillslopes at the Landscape Evolution Observatory (LEO) [*Gevaert et al.*, 2014], a research infrastructure managed by the University of Arizona at the Biosphere 2, Oracle, U.S.A. that comprises three identical convergent artificial hillslopes constructed with the aim of advancing

our predictive understanding of the coupled physical, chemical, biological, and geological processes at Earth's surface. The experiment experienced both saturation excess overland flow and outflow from the vertical downslope plane and thus required both a surface outlet and a dynamic seepage face boundary to be reproduced [*Niu et al.*, 2014].

Even in absence of vertical downslope planes (e.g., sharp riverbanks), seepage face conditions can arise, for instance, in riparian zones at the transition between hillslope and channel terrain or at higher elevation due to upward hydraulic gradients associated with subsurface flow convergence and geologic layering [e.g., *Mirus et al.*, 2007]. For these cases a consistent modeling treatment of outlet, atmospheric, and seepage face boundary conditions is needed. The complexities in this case originate from the diversity of runoff generation mechanisms (infiltration excess runoff, saturation excess runoff, return flow) and overland flow dynamics, including re-infiltration, ponding, and direct seepage to the stream channel [*Freeze*, 1974; *Beven and Wood*, 1983]. Simple models of saturation excess runoff are of the conceptual, lumped-parameter type [e.g., *Boughton*, 1990; *Willgoose and Perera*, 2001]. The saturation mechanism has also been widely investigated with the use of subsurface flow numerical models [e.g., *Beven*, 1977; *Ogden and Watts*, 2000; *Cloke et al.*, 2003]. More recently, *Beaugendre et al.* [2006] simulated water exfiltration at the ground surface with a coupled surface/subsurface model and compared the results with those obtained by using a simpler subsurface seepage face model. They show how, for simple scenarios involving constant slope and rainfall, the two approaches yield similar results. However, in their analysis re-infiltration processes are neglected.

In this study, we address the following four groups of questions relating the behavior of seepage face boundary conditions:

1. When is it acceptable to use a simpler, static (Dirichlet boundary condition) treatment of a seepage boundary in lieu of a dynamic (seepage face boundary condition) treatment? What are the approximation errors when using the simpler approach?
2. How do we resolve seepage face outflow under conditions of heterogeneity? What are the resulting dynamics?
3. In the context of integrated surface/subsurface modeling, how does a seepage face boundary interact with the catchment outlet boundary condition used in overland and channel flow models? Can the two types of boundary condition coexist?
4. What are the effects of re-infiltration processes when simulating water exfiltration at the land surface and overland flow? What is the relationship between the treatment of seepage face and atmospheric boundary conditions?

To answer these questions, we use the numerical model CATHY [*Camporese et al.*, 2010], which couples a finite element solver for 3-D subsurface flow with a finite difference solver for overland and channel routing. The original algorithm that handles the seepage face boundary condition in CATHY derives from the approach proposed by *Neuman* [1973] and is based on a single exit point whose position is updated during each nonlinear iteration of the Picard scheme that is used to solve the nonlinear Richards equation [*Paniconi and Putti*, 1994]. Here we propose a generalization of this approach that simplifies the classic algorithm and that deals also with multiple seepage faces in the presence of layered and random heterogeneity. The new algorithm extends other approaches, such as the one proposed by *Rulon and Freeze* [1985], in performing the update at each nonlinear iteration and in allowing the presence of more than two seepage faces. In the case where a seepage face occurs along a vertical downslope plane (as in classic hillslope or sloping aquifer configurations), any of the Richards equation-based integrated models mentioned earlier (HGS, ParFlow, etc) would use a boundary condition treatment similar to CATHY. When the seepage face occurs along a portion of the land surface, the different coupling approaches used, ranging from first-order exchange formulations to free surface and boundary condition methods [*Kollet et al.*, 2016], each has its own way of resolving the flow interactions. For instance, *Ebel et al.* [2009] and *Liggett et al.* [2012, 2013] have investigated the sensitivity of overland flow generation mechanisms to the first-order exchange coefficient, focusing mainly on Hortonian processes.

The simulations to address points 1 and 2 above are performed for a simple rectangular hillslope. Different scenarios are tested by changing the soil parameterization, the slope, and the atmospheric and initial conditions. The tests are designed to first analyze the approximation errors committed when modeling the outflow from the base of the hillslope as a simple fixed Dirichlet condition instead of as a dynamic seepage

face boundary condition (both options are available in the CATHY model). Second, the tests are used to examine the water table configurations and the dynamics of the different seepage faces and exit points arising from the presence of layered heterogeneity. To analyze the seepage face and surface outlet interactions (point 3), we consider a numerical model of the artificial hillslope constructed for the LEO project at Biosphere 2. In this real scenario, we look at the steady state rainfall partitioning between seepage face flow and surface outflow for different combinations of rainfall rate and average slope. The last set of simulations, addressing point 4, are run for a rectangular hillslope and are used to investigate the behavior of seepage face conditions for complex runoff generation and routing scenarios. These last test cases, featuring subsurface and coupled processes, are highly relevant for testing the handling of complex boundary conditions in integrated hydrological models. An incorrect representation and resolution of, for example, riverbank outflow, return flow, and rainfall-runoff partitioning can easily introduce approximation and mass balance errors that affect the overall numerical solution and model performance.

2. Methodology

2.1. Hydrological Model

CATHY (CATchment HYdrology) is a distributed physically based model that couples Richards' equation, describing flow in variably saturated porous media, and a finite difference solver for the diffusion wave equation, describing flow propagation over the land surface (overland runoff) and in the stream network (channel flow) [*Camporese et al.*, 2010]. The mathematical model consists of the following system of two partial differential equations:

$$S_w(\psi)S_s\frac{\partial \psi}{\partial t} + \phi\frac{\partial S_w}{\partial t} = \nabla \cdot [K_r(\psi)K_s(\nabla\psi + \eta_z)] + q_{ss} \tag{1a}$$

$$\frac{\partial Q}{\partial t} + c_k\frac{\partial Q}{\partial s} = D_h\frac{\partial^2 Q}{\partial s^2} + c_k q_s \tag{1b}$$

where in equation (1a) $S_w(\psi)$ $[L^3L^{-3}]$ is the water saturation, S_s $[L^{-1}]$ is the aquifer specific storage, ψ $[L]$ is the pressure head, $t[T]$ is time, ϕ $[L^3L^{-3}]$ is the porosity, K_s $[LT^{-1}]$ is the saturated hydraulic conductivity tensor, $K_r(\psi)$ is the relative hydraulic conductivity function, $\eta_z = (0, 0, 1)'$ with z $[L]$ the vertical coordinate directed upward, and q_{ss} $[L^3L^{-3}T^{-1}]$ is a source or sink term that includes the exchange fluxes from the surface to the subsurface. From S_w and ϕ the volumetric water content is defined as $\theta = S_w\phi$ $[L^3L^{-3}]$. In the surface flow equation (1b), Q $[L^3T^{-1}]$ is the discharge along the overland and channel network, c_k $[LT^{-1}]$ is the kinematic celerity, s $[L]$ is the coordinate direction for each segment of the overland and channel network, D_h $[L^2T^{-1}]$ is the hydraulic diffusivity, and q_s $[L^3L^{-1}T^{-1}]$ is the inflow or outflow rate from the subsurface to the surface.

The 3-D Richards equation is discretized by a P1 Galerkin finite element scheme in space using tetrahedral elements and by a backward Euler scheme in time with adaptive time step. The resulting system of nonlinear equations is linearized by the Picard iterative scheme [*Paniconi and Putti*, 1994]. The nonlinear characteristics $S_w(\psi)$ and $K_r(\psi)$ are specified using *van Genuchten* [1980] relationships. The stream channel network for surface flow propagation is identified using the terrain topography and the hydraulic geometry concept, and the equation is solved numerically using the Muskingum-Cunge method [*Orlandini and Rosso*, 1996, 1998].

The time-splitting algorithm that couples equations (1a) and (1b) proceeds as follows. The surface routing module propagates the surface water levels from time t^k to t^{k+1} and evaluates the surface to subsurface exchange fluxes q_{ss} at time t^{k+1}. Atmospheric inputs (rainfall or potential evaporation) and the q_{ss} fluxes are then partitioned into effective rainfall or evaporation and surface ponding via a boundary condition switching procedure during the Richards equation solution phase [*Camporese et al.*, 2010]. A mass balance calculation is used to determine the subsurface to surface exchange fluxes q_s at time t^{k+1}. Additional details on the model features and numerics can be found in *Camporese et al.* [2010] and *Paniconi and Putti* [1994].

2.2. Seepage Face Boundary Condition

A seepage face is the boundary between a saturated flow field and the atmosphere or a stream channel, typically modeled as a lateral boundary (e.g., a riverbank) where water is free to exit from the domain in
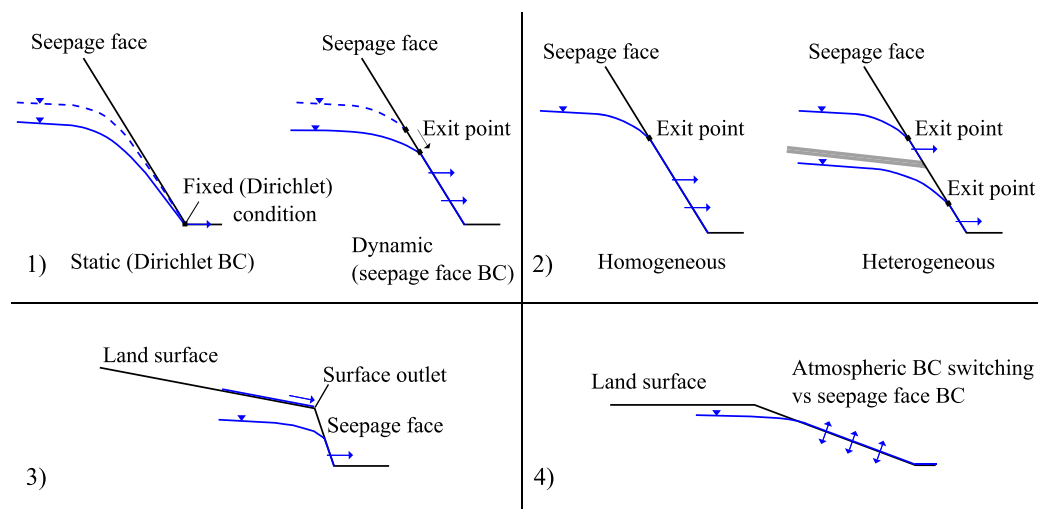
Figure 1. Conceptual representation of the boundary conditions (BC) implemented for the four analyses performed.

case of saturation. A seepage face can also form on portions of the land surface, such as along a gently sloping riparian zone. In the case of homogeneous porous media the exit point of a seepage face separates the saturated zone from the tension-saturated and unsaturated flow fields: below the exit point groundwater discharges at atmospheric pressure, while on the portion of the boundary above the exit point, which includes also the capillary fringe, there is no outflow. This definition needs to be generalized for heterogeneous cases, where several exit points may occur, as shown in case 2 of Figure 1. The seepage face is a dynamic boundary since for unsteady flow the exit point position changes in time, typically rising when the aquifer is recharging and dropping as the aquifer drains. The exit point position cannot be imposed a priori but rather is determined by the internal system state, i.e., by the level of the water table as it intersects the land surface.

For homogeneous porous media, the standard approach to handling dynamic seepage face boundary conditions in numerical models of variably saturated subsurface flow is described in numerous classic studies [e.g., *Neuman*, 1973; *Cooley*, 1983; *Huyakorn et al.*, 1986]. Here we propose a simplification and a generalization of this classic algorithm.

2.2.1. Standard Algorithm

In the classic approach, the nodes of the computational mesh forming the seepage face boundary are subdivided into distinct vertical or inclined lines. The nodes on each line are reordered in a consecutive way, from the bottom to the top, in such a way as to easily identify the exit point position along the vertical. The algorithm computes the exit point position at each iteration of the nonlinear scheme. For each seepage face line, the initial position of the exit point is calculated considering the initial ψ distribution: by checking the pressure from bottom to top, the exit point is set below the first node with negative ψ (atmospheric pressure is taken to be zero). As boundary condition for the next iteration the algorithm sets zero pressure head (Dirichlet condition) at the exit point and all nodes below it, and zero flux (Neumann condition) at the nodes above the exit point. At each nonlinear iteration the position of the exit point is adjusted based on the evolving ψ solution and the computed fluxes at the Dirichlet nodes. If an unphysical positive flux (inflow) is encountered at a node below the exit point, the exit point position is lowered for the next iteration. On the other hand, if a positive value of ψ is encountered at a node above the exit point, its position is raised. In CATHY, the user is given two options for identifying the new position of the exit point. In the first option, the seepage face convergence can be added as an additional constraint on convergence of the subsurface solver. If this option is selected, the subsurface solver converges, and thus can progress to the next time step, if both the Picard scheme converges and the exit points on all seepage lines are unchanged between the previous and current iterations. The second option proposes an alternative search for the new exit point by raising or lowering by only one node the exit point computed at the previous nonlinear

iteration. For the numerical tests performed in this study, the standard seepage face algorithm with either of the two options produced largely similar results.

The standard algorithm for modeling dynamic seepage face boundaries is particularly suited to vertically structured computational grids. In this configuration, the number of nodes to consider in the identification of the new exit point can be notably reduced if the search starts from the position of the exit point at the previous iteration. In addition to allowing handling of multiple exit points, the generalization of the dynamic seepage face algorithm proposed next can also be applied to unstructured 3-D grids, i.e., grids where it may not be possible to decompose a seepage face boundary into distinct lines.

2.2.2. Generalized Approach

In the generalized approach, the seepage face handling is greatly simplified by doing away with the notion of individual seepage face lines and the consequent ordering of nodes by elevation. In fact, the new algorithm only requires identification of the nodes belonging to the seepage outflow plane, without any additional ordering based on elevation or lateral position. At the start of the simulation and after every nonlinear iteration, the Dirichlet or Neumann assignation is performed according to the same procedure used in the classic algorithm, but without following a bottom to top (or any other) order. Instead of focusing on the identification of the exit points, the new algorithm simply finds the "active" nodes of the seepage face boundary by checking node by node for the presence of positive pressures with an associated outflow (i.e., the Dirichlet nodes). Once this operation is performed, it is possible (but not necessary for the computation of the numerical solution at the next iteration) to identify the active portions of the seepage face boundary by grouping the contiguous Dirichlet boundaries (contiguous nodes along the seepage face having a Dirichlet condition). With this idea the exit points can be associated to the nodes at the highest elevations of an active portion.

In addition to its simplicity of implementation and its suitability for unstructured grids, the new algorithm automatically handles multiple seepage faces in the presence of layered and random heterogeneity, and it reveals similarities between the way seepage face and atmospheric boundary conditions are handled that are not as apparent in the classic formulation.

2.3. Setup of Numerical Experiments

We perform four analyses: in the first set we look at the difference between treating a seepage face as a static (Dirichlet) or dynamic (according to the algorithms presented in section 2.2) boundary (case 1 in Figure 1); in the second, we study the seepage face response in the presence of layered heterogeneity (case 2 in Figure 1); in the third, we analyze the interactions between the seepage face and surface outlet (case 3 in Figure 1); and finally we investigate possible similarities between seepage face and atmospheric boundary condition switching algorithms for cases where seepage faces form on portions of the land surface (case 4 in Figure 1). Table 1 summarizes the parameter combinations and setup for each simulation performed in the four sets of experiments. In the first set, which features a homogeneous domain, we also verified that the classic and generalized seepage face algorithms give the same results.

2.3.1. Static Versus Dynamic Treatment of the Seepage Boundary

One common and easy way to treat a seepage face is to set to 0 (atmospheric pressure) the pressure head at the bottom of the outflow plane (i.e., a fixed Dirichlet boundary condition) and to 0 the flux on all the other nodes of the plane (i.e., a no-flow Neumann boundary condition). This static treatment of the seepage face boundary can lead to large approximation errors since the actual exit point can be elsewhere than at the bottom, and its position can vary greatly during the course of a simulation. To investigate these errors, we compare the results obtained with the static Dirichlet treatment with those from the dynamic seepage face algorithm. The comparison is performed on the synthetic rectangular sloping aquifer depicted in Figure 2a. The domain is 10 m long, 1 m deep, and 1 m wide and is discretized into 100×5 grid cells in the lateral direction and 50 layers of equal thickness in the vertical direction. The bottom of the aquifer as well as all lateral boundaries except for the downslope outflow plane is assigned no-flow conditions. We perform simulations during which the hillslope drains water out through the outflow plane from fully saturated initial conditions (drainage test cases) and from initially dry conditions subjected to constant rainfall.

For the drainage runs we set no-flow conditions at the land surface to preempt overland flow. The initial pressure head is hydrostatically distributed with the water table at the surface. The approximation error at time t is quantified as:

Table 1. Parameter Values for the Four Sets of Numerical Experiments[a]

Numerical Experiment		Saturated Hydraulic Conductivity K_s (m/s)		Aquifer Slope i (%)	Rainfall R (m/s)
Static (Dirichlet boundary conditions)	Drainage simulations	1×10^{-3}		10	0
		1×10^{-4}		10	0
		1×10^{-5}		10	0
versus		1×10^{-4}		1	0
Dynamic (seepage face boundary conditions)		1×10^{-4}		30	0
	Rainfall simulations	1×10^{-4}		10	$0.025–0.5 \times 10^{-4}$
		1×10^{-5}		10	$0.025–0.5 \times 10^{-5}$
		1×10^{-4}		1	$0.025–0.5 \times 10^{-4}$
		1×10^{-4}		30	$0.025–0.5 \times 10^{-4}$
		Top Layer K_{s1}	Bottom Layer K_{s2}		
Layered heterogeneity	Two-layer	1×10^{-4}	1×10^{-5}	10	0
		1×10^{-4}	1×10^{-6}	10	0
		1×10^{-5}	1×10^{-4}	10	0
		1×10^{-6}	1×10^{-4}	10	0
		1×10^{-4}	1×10^{-5}	10	1×10^{-5}
		1×10^{-4}	1×10^{-6}	10	1×10^{-5}
		1×10^{-5}	1×10^{-4}	10	1×10^{-6}
		1×10^{-6}	1×10^{-4}	10	1×10^{-7}
		Soil K_s	Lens K_{sL}		
	Single-layer with impeding lens	1×10^{-4}	1×10^{-6}	10	1×10^{-5}
		1×10^{-4}	1×10^{-8}	10	1×10^{-5}
	Multiple-layer	K_{s1} K_{s2} K_{s3} K_{s4} 1×10^{-4} 1×10^{-6} 1×10^{-4} 1×10^{-6}		10	1×10^{-5}
		Soil Hydraulic Conductivity K_s (m/s)			
Seepage face and surface outlet interactions		1×10^{-4}		3	$0.0015–1.5 \times 10^{-4}$
		1×10^{-4}		10	$0.0015–1.5 \times 10^{-4}$
		1×10^{-4}		20	$0.0015–1.5 \times 10^{-4}$
					i_b (%)
Seepage face boundary condition		1×10^{-4}		20	1.5×10^{-6}
versus		1×10^{-4}		50	1.5×10^{-6}
atmospheric boundary condition switching		1×10^{-4}		100	1.5×10^{-6}

[a]The initial position of the water table for the simulations with rainfall is at the bottom of the domain, while for the simulations with zero rainfall it is at the surface.

$$\epsilon^D(t) = \frac{|V_{st}(t) - V_{dy}(t)|}{V_{dy}(t)} \times 100 \tag{2}$$

where $V_{dy}(t)$ and $V_{st}(t)$ are the cumulative outflow volumes from, respectively, the dynamic and static cases. Different combinations of saturated hydraulic conductivity ($K_s = 1 \times 10^{-3}$, 1×10^{-4}, and 1×10^{-5} m/s) and slope angle ($i = 1\%$, 10%, and 30%) were run (see Table 1).

For the rainfall tests, we set atmospheric conditions at the land surface with a constant rainfall rate. The initial pressure head is hydrostatically distributed with the water table at the bottom of the domain. The approximation error is quantified as:

$$\epsilon^R = \frac{|Q_{st}^{ss} - Q_{dy}^{ss}|}{Q_{dy}^{ss}} \times 100 \tag{3}$$

where Q_{dy}^{ss} and Q_{st}^{ss} are the steady state volumetric flow raised from, respectively, the dynamic and static cases. The different parameter combinations included slope angles of 1%, 10%, and 30%, saturated hydraulic conductivities of 1×10^{-4} and 1×10^{-5} m/s, and rainfall rate R set in such a way that a ratio R/K_s between 0.025 and 0.5 was sampled for each slope angle and K_s combination (see Table 1).

2.3.2. Layered Heterogeneity

For the layered heterogeneity analysis, we again use the domain depicted in Figure 2a, with fixed slope $i = 10\%$. A seepage face boundary is set on the downslope outflow plane, atmospheric conditions are set on the surface boundary during rainfall, otherwise no-flow conditions are set, and no-flow conditions are set on all the other boundaries. We run three sets of simulations: two-layer, single-layer with impeding lens,
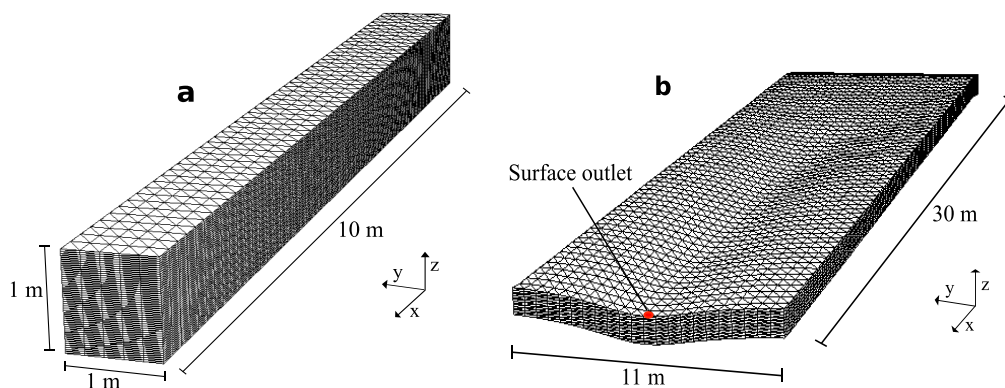
Figure 2. (a) 3-D numerical grid for the rectangular sloping aquifer and (b) for the LEO hillslope.

and multiple-layer heterogeneity (Figure 3), in the first set under both drainage and rainfall conditions and in the other two sets under rainfall conditions only. The initial water table position for all drainage runs was at the land surface (with no-flow conditions at the surface to preempt overland flow), whereas for all rainfall runs it was at the bottom of the domain. All simulations were run to steady state.

For the two-layer test case the ratio of upper layer K_{s1} to lower layer K_{s2} hydraulic conductivity was set to 100, 10, 0.1, and 0.01. In the rainfall runs, the rain rate was set to one order of magnitude less than K_{s1}. For the impeding lens test case the lens conductivity K_{sL} was set to 2 and 4 orders of magnitude lower than the soil K_s conductivity. The rainfall rate was again one order of magnitude less than K_s. The multiple-layer test case featured four layers of equal thickness and of conductivity (top to bottom) 1×10^{-4}, 1×10^{-6}, 1×10^{-4}, and 1×10^{-6} m/s and a rainfall rate of 1×10^{-5} m/s. The parameter values for these various configurations are summarized in Table 1.

2.3.3. Seepage Face and Surface Outlet Interactions
In this analysis, we look at the scenarios arising in the presence of both a seepage face and a surface outlet. To perform the simulations, we consider the LEO model (Figure 2b). This is a 30 m long, 1 m deep, and 11 m wide convergent landscape and is discretized into 22 × 60 grid cells in the lateral direction and 10
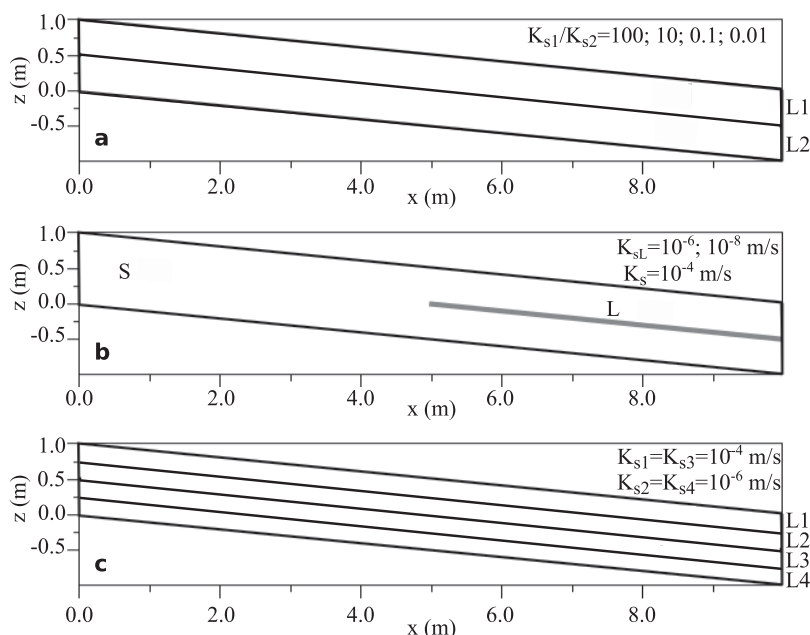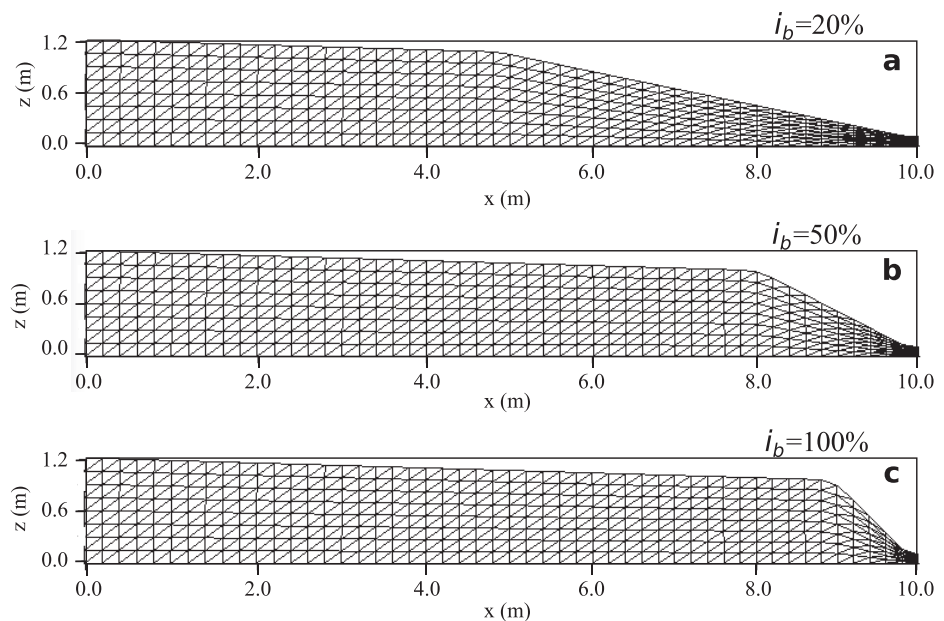

Figure 3. Vertical cross section of the sloping aquifer for the (a) two-layer, (b) single-layer with impeding lens, and (c) multiple-layer configurations, showing the hydraulic conductivity values or ratios used in each case.

Figure 4. Vertical cross section and computational mesh of the domain used in the three numerical experiments for the seepage face versus atmospheric conditions analysis.

layers of equal thickness in the vertical direction. We set atmospheric conditions at the surface boundary, a seepage boundary on the downslope vertical plane (the nodes that intersect this plane and the land surface are designated as atmospheric nodes), and no-flow conditions at the bottom boundary and along the three other lateral boundaries. The catchment outlet for the CATHY surface routing model is the land surface cell shown in red in Figure 2b. We set the hydraulic conductivity K_s of the system to 1×10^{-4} m/s and initially the water table at bottom with (negative) pressure head hydrostatically distributed. We ran simulations for a range of rainfall rates such that R/K_s ranged from 0.005 to 1.5, and for slope angles i of 3%, 10%, and 20%. Table 1 summarizes these configurations. The analysis is based on examination of the rainfall partitioning at steady state between seepage face flow Q_{sf} and surface flow Q, considering that when the process is at steady state the change in total water storage is zero and the total inflow (R) is equal to the total outflow ($Q_{sf} + Q$).
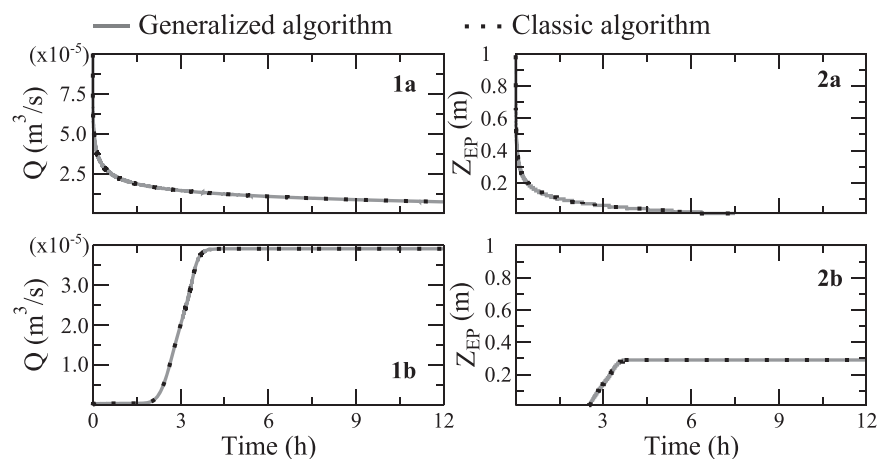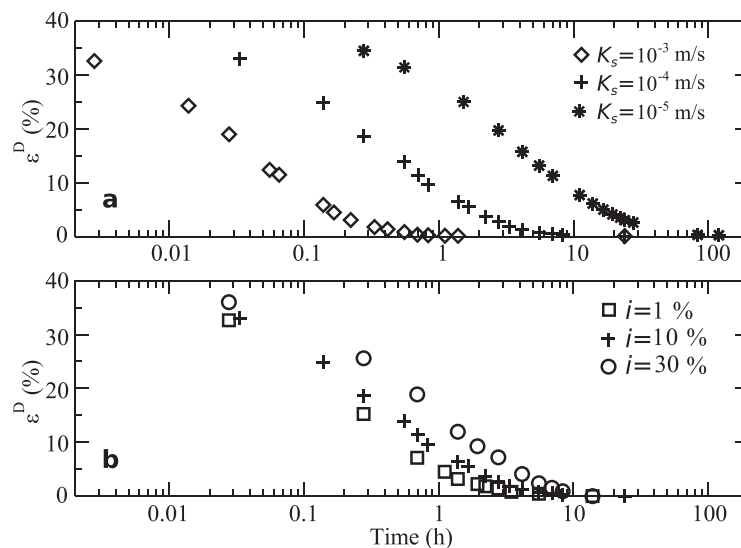

Figure 5. Results obtained with the classic and generalized seepage face boundary condition algorithms for a drainage simulation (panels a) and (panels b) a rainfall simulation showing the seepage face volumetric outflow Q (panels 1) and the exit point height Z_{EP} from the bottom (panels 2). The simulations are for a homogeneous sloping aquifer with hydraulic conductivity $K_s = 1 \times 10^{-4}$ m/s, inclination $i = 10\%$, and, for the rainfall case, $R = 1 \times 10^{-5}$ m/s.
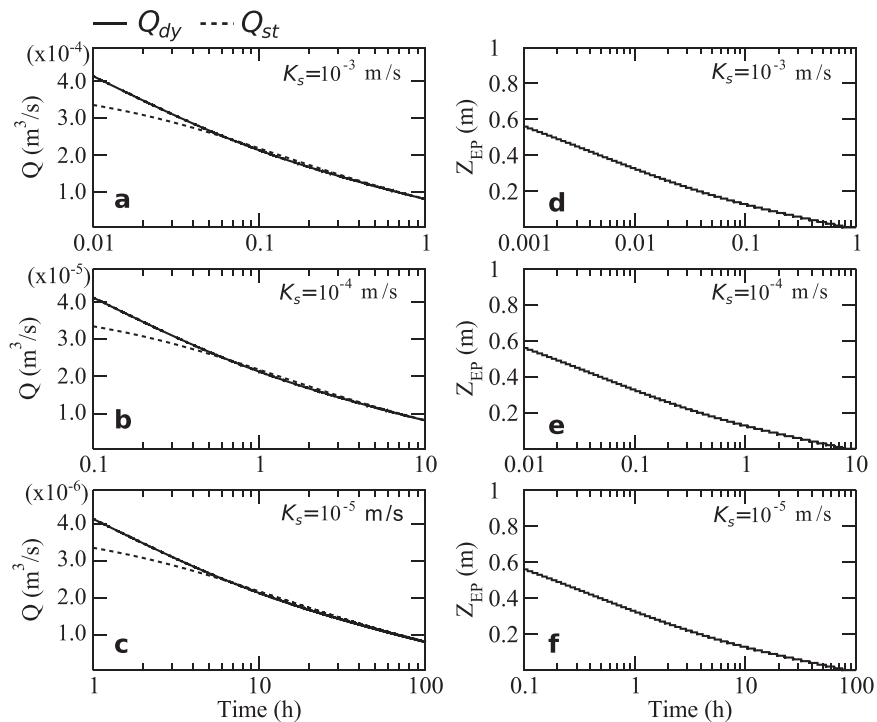
Figure 6. Results for the drainage simulations with a homogeneous sloping aquifer of inclination 10% and varying hydraulic conductivity K_s. (a–c) Volumetric outflow for static (Q_{st}) and dynamic (Q_{dy}) treatment of the seepage face boundary; (d–f) exit point height Z_{EP} for the dynamic treatment case.
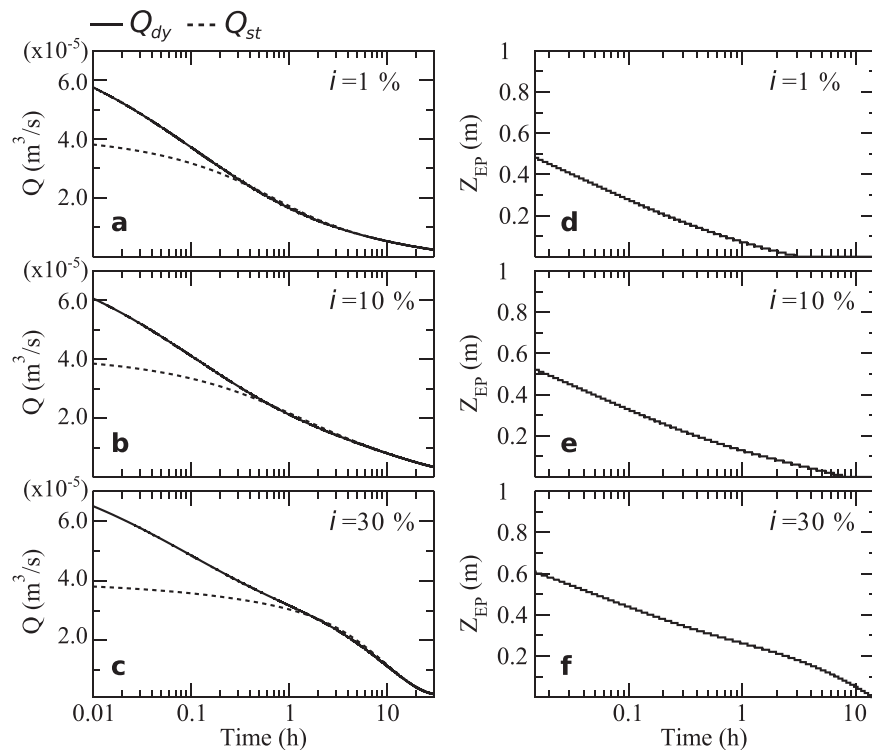
2.3.4. Seepage Face Versus Atmospheric Conditions

Seepage faces forming on portions of the land surface can be modeled either with a seepage face condition or via atmospheric boundary condition switching. In this analysis, we assess the differences between these two approaches. The comparison is performed on the three domains shown in Figure 4 that are 10 m long, 1.2 m deep (at the upslope boundary), and 1 m wide and are discretized into 50 × 5 grid cells in the lateral direction and eight layers of varying thickness. The i_b values of 20%, 50%, and 100% indicated in Figure 4 are the slope angles of the downslope 5, 2, and 1 m portions, respectively, of hillslopes a, b, and c. On this portion of the land surface, we set either atmospheric conditions or seepage face conditions, and zero rainfall to avoid the need to perform a mass balance calculation in the seepage face algorithm. On the remaining portion of the land surface (upslope 5, 8, and 9 m, respectively, of hillslopes a, b, and c) we set a constant rainfall rate of 1.5 $\times 10^{-6}$ m/s (this was found to be a maximal rate applicable to all three hillslopes that avoids generating runoff on this portion of the land surface). All lateral boundaries and the bottom boundary are assigned a no-flow condition. The hydraulic conductivity is

Figure 7. (a) Approximation error ϵ^D over time for the drainage simulations with a homogeneous sloping aquifer of inclination 10% and varying hydraulic conductivity K_s and (b) of hydraulic conductivity $K_s = 1 \times 10^{-4}$ m/s and varying inclination i.

Figure 8. Results for the drainage simulations with a homogeneous sloping aquifer of hydraulic conductivity $K_s = 1 \times 10^{-4}$ m/s and varying inclination i. (a–c) Volumetric outflow for static (Q_{st}) and dynamic (Q_{dy}) treatment of the seepage face boundary; (d–f) exit point height Z_{EP} for the dynamic treatment case.

set to 1×10^{-4} m/s and the water table initially at bottom with pressure head hydrostatically distributed (Table 1). The simulations are run until steady state. The atmospheric case is simulated in three ways: with CATHY in subsurface-only mode (any exfiltration leaves the domain instantaneously; ponding and re-infiltration cannot occur); in coupled mode (exfiltrating water can produce ponding and overland flow, and can re-infiltrate); and in coupled mode but with very high kinematic celerity (this very fast surface routing case should in principle approach the subsurface-only case). In the two coupled cases, the outlet cell for the surface routing model is situated at the intersection of the downslope vertical plane and the land surface, at the center of the hillslope in the transverse direction. We examine the differences over time between the seepage face volumetric flow and the exfiltration volumetric flow (for the subsurface-only atmospheric case) and outlet atmospheric flow (for the coupled case), as well as the differences in water table distance from the outlet, X_{WT}, calculated by averaging along the transverse direction.
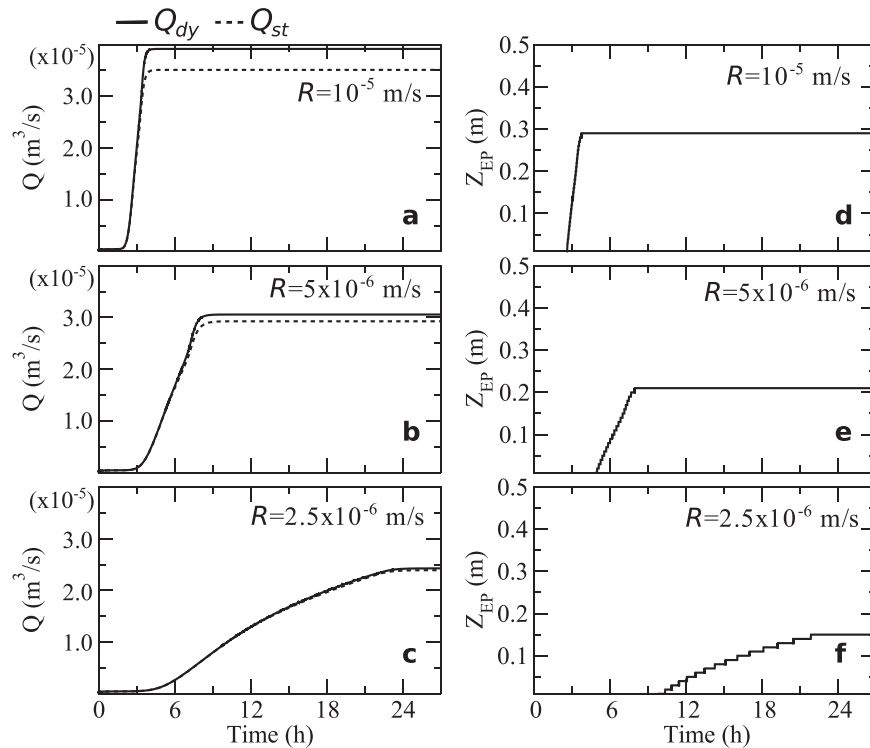
3. Results

For all the simulations involving homogeneous conditions, we first verified that the generalized and classic seepage face boundary condition algorithms gave the same results. Figure 5 reports the comparison for a drainage and a rainfall test case summarized in Table 1 ($K_s = 1 \times 10^{-4}$ m/s, $i = 10\%$, $R = 1 \times 10^{-5}$ m/s for the rainfall case), and it can be seen that the dynamics of the seepage face outflow Q and exit point height Z_{EP} (measured from the bottom of the domain) are identical. This was confirmed for all the other homogeneous test cases.

3.1. Static Versus Dynamic Treatment of the Seepage Boundary
### 3.1.1. Drainage Simulations
The results of the drainage simulations for the static versus dynamic treatment of the seepage boundary are shown in Figures 6 and 7. The results show that the volumetric outflow obtained for the dynamic treatment (Q_{dy}) is higher than the one obtained for the static treatment (Q_{st}) early in the simulation, that the

Figure 9. Results of the rainfall simulations with a homogeneous sloping aquifer of inclination 10%, hydraulic conductivity 1×10^{-4} m/s, and varying rainfall rate R. (a–c) Volumetric outflow for static (Q_{st}) and dynamic (Q_{dy}) treatment of the seepage boundary; (d–f) exit point height Z_{EP} for the dynamic treatment case.

differences diminish over time, and that the solutions converge by the time the position of the exit point for the dynamic treatment case converges to the position of the Dirichlet node, at the bottom of the domain (Figure 6). From the scaling of the time axis in Figure 6, it is also apparent that, all other parameters being equal, the seepage outflow response for both boundary condition treatments and the exit point response for the dynamic case scale exactly with hydraulic conductivity K_s. In Figure 7, we plot over time the approximation error ϵ^D (equation (2)) for the various K_s simulations at fixed slope angle (Figure 7a) and for the various slope cases at fixed K_s (Figure 7b). Here we see that the error committed using a static treatment for the seepage boundary rather than a dynamic treatment can be quite high (about 35% for all runs) early in the simulation, and falls to zero by the end of the simulation. The time to convergence (zero error) scales with K_s for
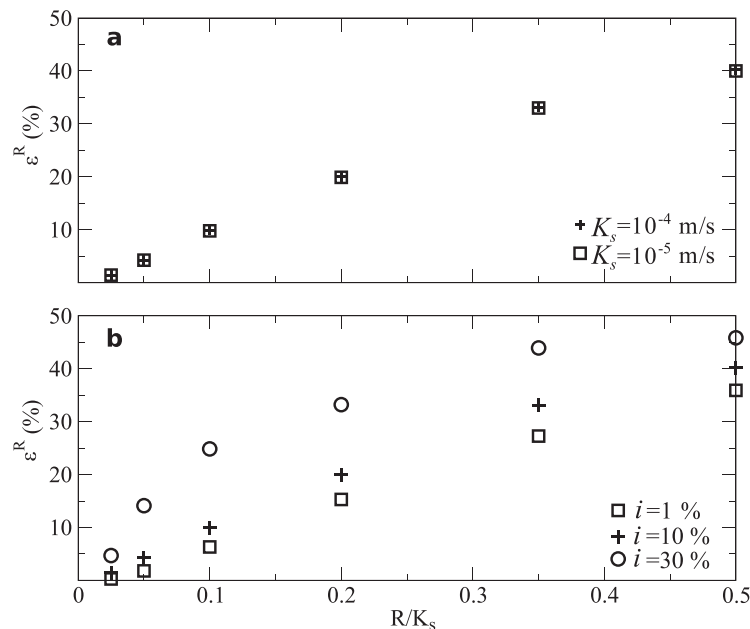
Figure 10. Approximation error ϵ^R as a function of rainfall/conductivity ratio R/K_s for the rainfall simulations with a homogeneous sloping aquifer of (a) inclination $i = 10\%$ and varying conductivity K_s and (b) conductivity $K_s = 1 \times 10^{-4}$ m/s and varying inclination i.
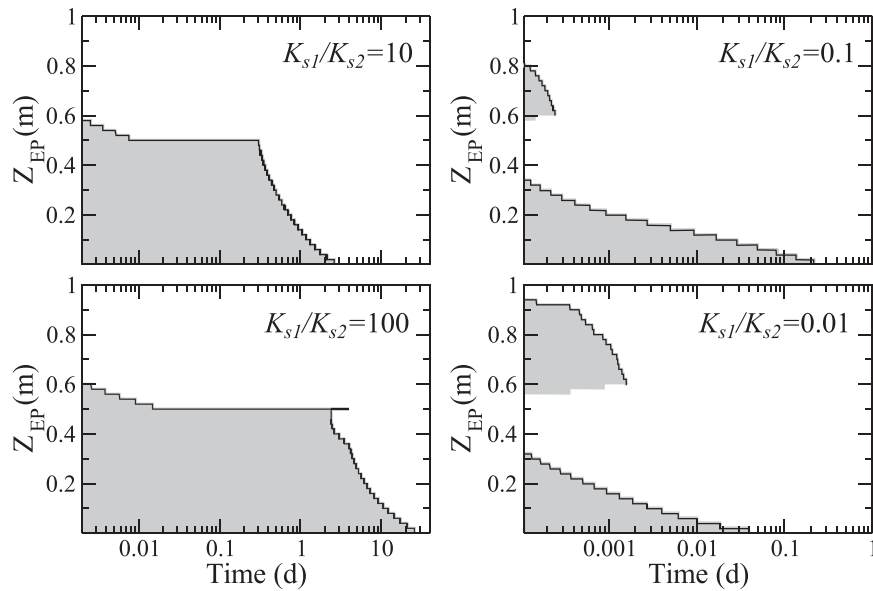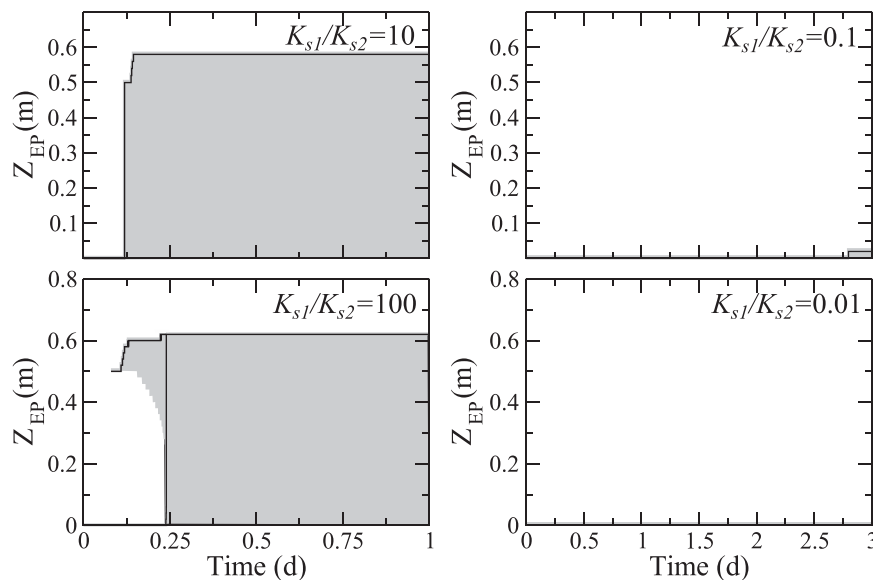
Figure 11. Evolution of the seepage face exit point height Z_{EP} for the two-layer drainage simulations with four different conductivity contrasts between the top (K_{s1}) and bottom (K_{s2}) layers. The shaded areas represent the seepage face outflow planes below each exit point.

the varying hydraulic conductivity runs (Figure 7a), as was pointed out also in Figure 6. For the varying slope runs, the time to convergence corresponds, as was the case also for the varying K_s runs, to the time required for the position of the exit point in the dynamic case to reach the bottom of the hillslope. This is shown in Figure 8. The time to convergence increases as the slope angle increases.

3.1.2. Rainfall Simulations
The results of the rainfall tests for the approximation errors committed when using a static boundary condition to model a seepage face are shown in Figures 9 and 10. For fixed K_s and fixed i, the differences between the two approaches increase with rainfall rate R, as does the final (steady state) position of the seepage face exit point (Figure 9). In Figure 10, we report the effects of (a) hydraulic conductivity K_s (fixed

Figure 12. Evolution of the seepage face exit point height Z_{EP} for the two-layer rainfall simulations with four different conductivity contrasts between the top (K_{s1}) and bottom (K_{s2}) layers. The shaded areas represent the seepage face outflow plots below each exit point.
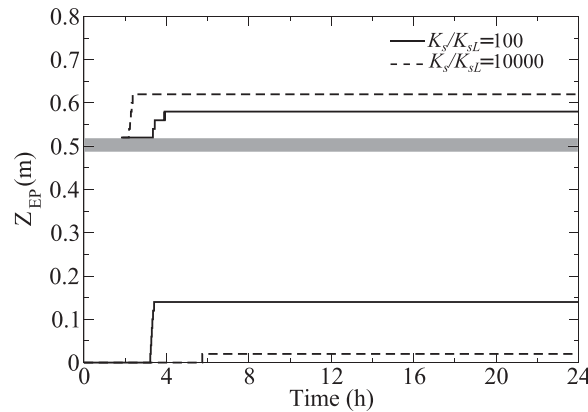
Figure 13. Evolution of the seepage face exit point height Z_{EP} above and below an impeding lens (shown as the gray strip) for two different conductivity contrasts between the aquifer (K_s) and the lens (K_{sL}).

$i = 10\%$) and (b) slope i (fixed $K_s = 1 \times 10^{-4}$ m/s) on the approximation errors ϵ^R calculated at steady state (equation (3)) for different ratios R/K_s. The error committed using a static treatment for the seepage boundary rather than a dynamic treatment increases significantly with R/K_s (reaching 45%), and also with i for fixed R/K_s. The error does not vary with K_s for a fixed R/K_s ratio.

On the basis of these drainage and rainfall tests, it can be concluded that the validity of the static treatment of a seepage boundary is restricted to very simple configurations, such as homogeneous, gently sloping aquifers under steady state conditions or subjected to low intensity forcing (rainfall). When applicable, simple configurations and a simple boundary condition can be amenable to analytical resolution, which can be very useful in hydrologic analyses [e.g., *Troch et al.*, 2013].

3.2. Layered Heterogeneity
3.2.1. Double Layers
The results of the simulations run for the two-layer hillslope configuration are shown in Figures 11 and 12. Under drainage from initial full saturation (Figure 11), the only case that does not feature a second exit point is $K_{s1}/K_{s2} = 10$. For $K_{s1}/K_{s2} = 100$, the position of the first exit point quickly drops from the surface to the interface between the two layers and after about 2 days it starts dropping toward the bottom (reached after about 25 days from the beginning of the simulation). At this time, a second exit point appears at the interface of the two layers and persists for about 2 days. Setting the hydraulic conductivity of the top layer one or two orders of magnitude smaller than that of the bottom layer also results in the formation of two seepage faces, but in this case the dual exit points occur very early in the simulation and the top seepage face has a very short duration (about 250 and 500 s, respectively, for the $K_{s1}/K_{s2} = 0.1$ and $K_{s1}/K_{s2} = 0.01$ cases).

For the rainfall simulations (Figure 12), the only case that features a second exit point is $K_{s1}/K_{s2} = 100$. For this case only one exit point, whose position Z_{EP} is at the bottom, is present from the beginning of the simulation until 2.5 h (0.1 day), at which time the infiltration front reaches the interface between the two layers and a second exit point develops. It initially sits at the interface and then rises to $Z_{EP} = 0.6$ m. After 6 h from the beginning of the simulation, the rainfall water reaches the bottom and, in turn, starts feeding the first
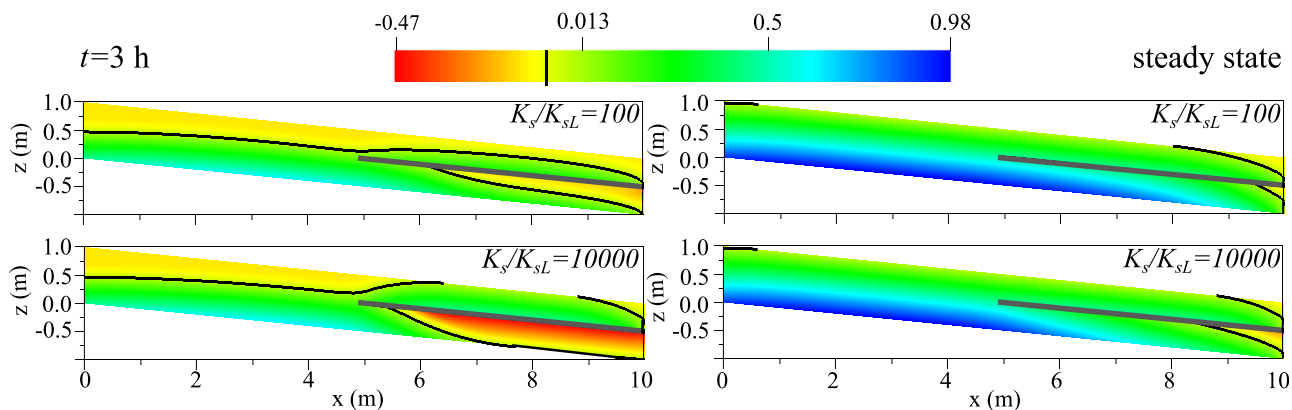
Figure 14. (left) Pressure head profiles (m) and zero pressure head contours (shown in black) in vertical cross section and at times 3 h and (right) steady state for the simulations with an impeding lens (shown in gray) with conductivity contrast between the aquifer (K_s) and the lens (K_{sL}) of (top) $K_s/K_{sL} = 100$ and (bottom) $K_s/K_{sL} = 10,000$.
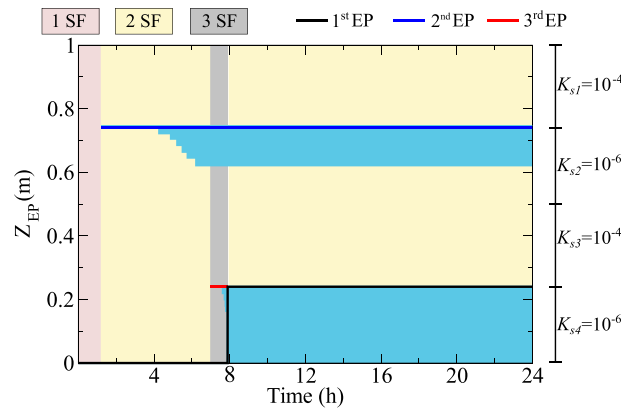
Figure 15. Dynamics of the first (black line), second (blue line), and third (red line) exit point (EP) for the multiple-layer test case. The seepage face (SF) outflow planes below each exit point are shown as the light-blue areas. The pink, yellow, and gray areas show the time spans during which, respectively, one SF, two SFs, and three SFs are present.

seepage face. As a consequence, the first exit point rapidly rises to reach the second exit point and the two seepage faces merge.

3.2.2. Single Layer With a Thin Impeding Lens

The results of the two simulations for the single-layer with impeding lens configuration (see Table 1) are shown in Figure 13. In both cases, a second exit point appears when the infiltration front reaches the impeding lens (at about 1.5 h from the beginning of the simulation). For the $K_s/K_{sL} = 10,000$ case this second exit point rises rapidly, while for the $K_s/K_{sL} = 100$ case more water is able to percolate across the impeding lens, making the second exit point rise more slowly.

The dynamics of the first seepage face is also different between these two permeability contrast cases. When $K_s/K_{sL} = 100$ the first exit point starts rising at 3.5 h whereas when $K_s/K_{sL} = 10,000$ the first seepage face can only be fed by rainfall water that drains from upslope (much less percolation through the lens), and as a consequence the first exit point starts rising only at 6 h. Not surprisingly, at steady state the heights of the first and second exit points are, respectively, higher and lower for $K_s/K_{sL} = 100$ than for $K_s/K_{sL} = 10,000$. In Figure 14, we compare the pressure head profile in vertical cross section at 3 h (about 1 h after the appearance of the second exit point) and at steady state. The profile at 3 h clearly shows that the soil below the lens is much wetter for the $K_s/K_{sL} = 100$ case, while the water table above the lens is more developed for the $K_s/K_{sL} = 10,000$ case. In both cases at steady state the soil below the lens is wet and two water tables are present, at bottom and above the lens.

3.2.3. Multiple Layers

The simulation performed for the multiple seepage face case features the presence of three seepage faces and corresponding exit points. Figure 15 shows their dynamics and in what follows we refer to the first, second, and third seepage face/exit point as they appeared chronologically. At the beginning only one seepage face with its exit point (black line in Figure 15) at bottom is present. A second seepage face develops when the infiltration front reaches layer 2 (at approximately 1.5 h). Its exit point (blue line) sits at the interface between the first two layers and neither rises nor falls for the duration of the simulation. A third seepage face forms when the
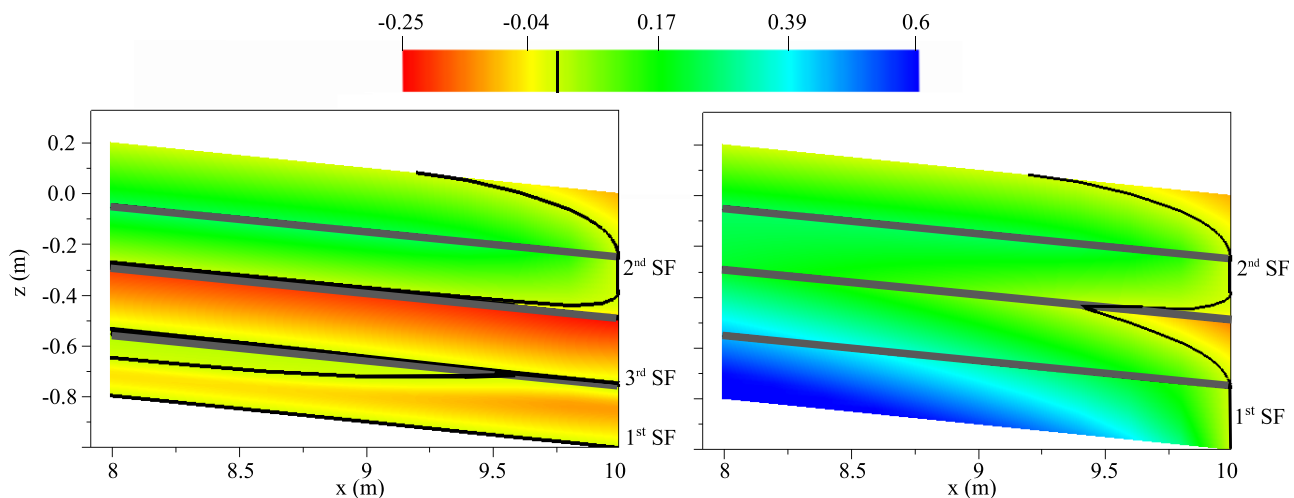
Figure 16. (left) Snapshots at 7 h and (right) at steady state of the profiles of pressure head (m) in vertical cross section at the downslope 2 m portion of the hillslope for the multiple-layer simulation. The interfaces between layers are shown by the gray lines while the contours of zero pressure head are traced by the black lines.
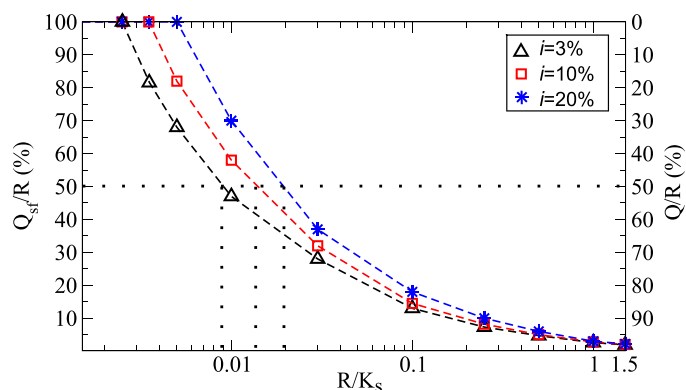
Figure 17. Partitioning of rainfall R on the LEO hillslope between seepage face outflow Q_{sf} (left axis) and surface outlet discharge Q (right axis) at steady state for a range of rainfall/conductivity (R/K_s) ratios and three different slope angles i. The horizontal and three vertical dotted lines give the R/K_s value at which seepage and outlet contributions are equal ($R/K_s = 0.009$, 0.012, and 0.02 for slope angles 3%, 10%, and 20%, respectively).

infiltration front reaches layer 4, at around 7 h, with its exit point (red line) at the interface between layers 3 and 4. At 8 h, the rainfall water reaches the bottom and the first exit point rises to the height of the third exit point such that the first and third seepage faces merge for the remainder of the simulation, to steady state. In Figure 16, we show the pressure head profile in vertical cross section for the downslope 2 m portion of the hillslope at 7 h, when three seepage faces are present, and at steady state. From the zero pressure head contours, shown as black lines, the different seepage faces are easily discerned. The profile at 7 h shows: the first seepage face at bottom, the second seepage face in layer 2 and at the interface between the first two layers, and the third seepage face at the interface between layers 3 and 4. The steady state profile shows: the first seepage face in layer 4 and at the interface between layers 3 and 4 and the second seepage face in a portion of layer 2 and at the interface between the first two layers.

3.3. Seepage Face and Surface Outlet Interactions

The results of a series of simulations on the LEO hillslope to examine seepage face and surface outlet interactions are presented in Figure 17 and show the steady state rainfall (R) partitioning between seepage face flow Q_{sf} and surface outflow Q for different ratios of R/K_s (the hydraulic conductivity was fixed at $K_s = 1 \times 10^{-4}$ m/s) and three slope angles i. The results show that the seepage face contribution Q_{sf}/R decreases with R/K_s and increases with i. Thus, higher rainfall rates enhance overland flow while steep slopes enhance flow from the base of the hillslope. They also show that the differences between the three slope angles become less significant as R/K_s increases. In addition, it is seen that the R/K_s value at which seepage face and outlet contributions are equal increases with i. Thus, the R/K_s range for which seepage face flow is
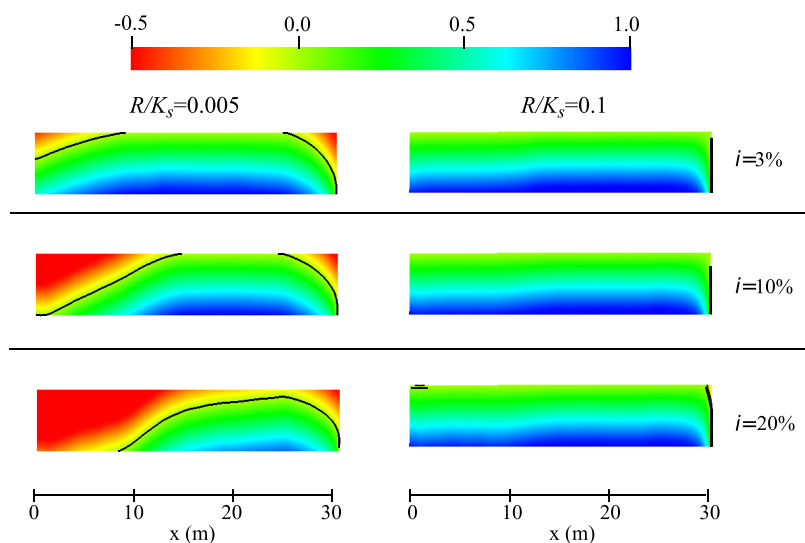

Figure 18. Steady state profiles of pressure head (m) (color map) and water table (black lines) for the LEO hillslope taken in vertical cross section along the x direction (midpoint in the y direction). The seepage boundary is at $x = 30$ m. The results are shown for two rainfall/conductivity (R/K_s) ratios and three slope angles i.
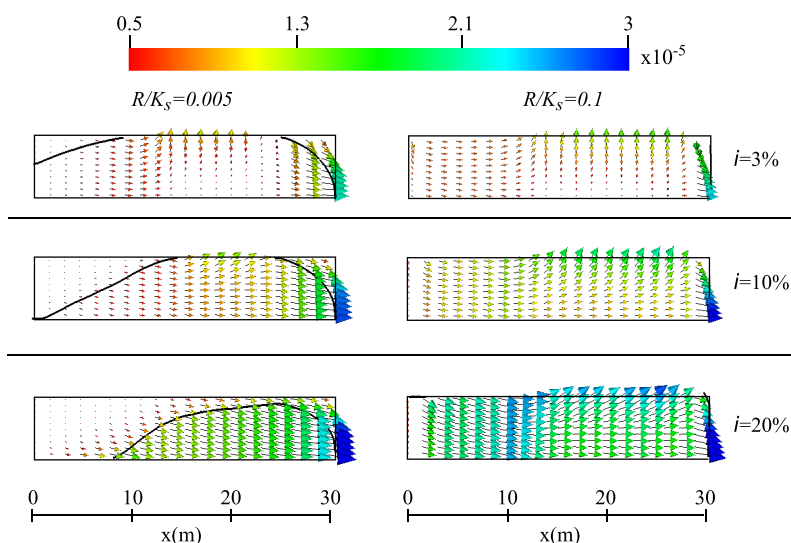
Figure 19. Steady state profiles of Darcy velocity for the LEO hillslope taken in vertical cross section along the x direction (midpoint in the y direction). The seepage boundary is at $x = 30$ m. The results are shown for two rainfall/conductivity (R/K_s) ratios and three slope angles i.

greater than surface flow increases with i. These results can be better understood by looking at the profiles shown in Figures 18 and 19. Here the steady state pressure head and velocity profiles for the different slopes are plotted for a case in which the seepage face contribution exceeds the surface flow contribution ($R/K_s = 0.005$) and for a case in which the surface flow contribution exceeds the seepage face contribution ($R/K_s = 0.1$). In accordance with what has been noted from Figure 17, the differences between profiles for the three different slope angles are greater for the $R/K_s = 0.005$ case than for the $R/K_s = 0.1$ case. The differences include a smaller portion of the land surface intersected by the water table, the water table mound further downslope, less water exfiltration at the land surface, and higher velocities at the seepage face for increasing i. In addition, while for the $R/K_s = 0.005$ case, where unsaturated areas persist for all three slopes
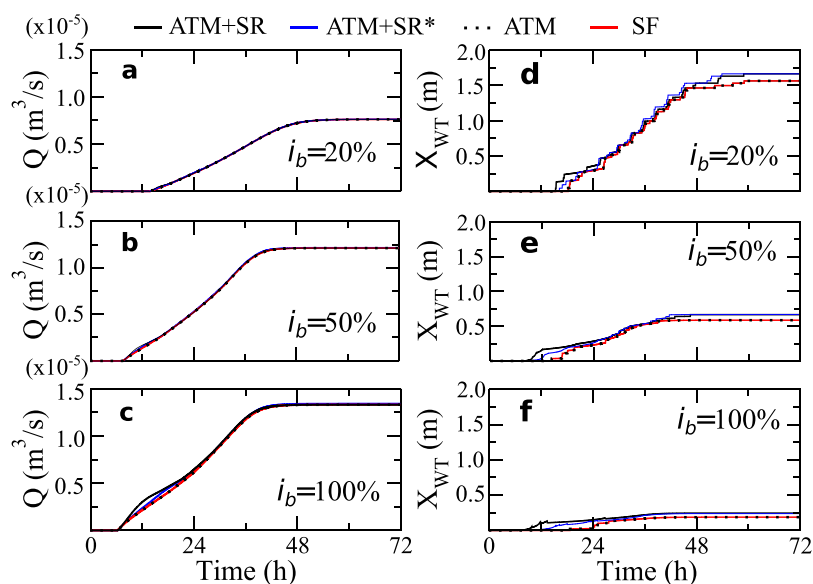
Figure 20. Results of the seepage face versus atmospheric conditions simulations with a homogeneous aquifer of hydraulic conductivity 1×10^{-4} m/s and different downslope land surface inclinations i_b. (a–c) Volumetric outflow Q over time from the land surface. (d–f) Average distance of the water table, X_{WT}, from the outlet. The results are shown for four different boundary condition treatments of the downslope portion (see Figure 4) of the test hillslopes: as a seepage face boundary condition (SF, red lines); as atmospheric boundary conditions in subsurface-only mode (ATM, dotted black lines); as atmospheric conditions in coupled mode, i.e., with surface routing (ATM + SR, solid black lines); and as atmospheric conditions in coupled mode with high kinematic celerity, i.e., with very fast routing (ATM + SR*, blue lines).

and most of the outflow is from the seepage face, the fully saturated conditions encountered for the $R/K_s = 0.1$ case give rise to enhanced convergent velocity trajectories toward the surface outlet.

3.4. Seepage Face Versus Atmospheric Conditions

The results of the simulations involving a seepage face forming at the land surface (for the hillslopes shown in Figure 4 and parameter values given in Table 1) are shown in Figure 20 for the four different boundary condition treatments in terms of the time behavior of the volumetric discharge flow Q outflowing from the downslope portion of the land surface and the average distance of the water table XW_T from the outlet. The ATM curves in Figure 20 coincide exactly with the SF curves for all three hillslopes and in both outflow and water table dynamics. The algorithms that handle boundary condition switching between Dirichlet and Neumann status that are used for land surface atmospheric forcing and for seepage faces are thus entirely consistent. When CATHY is run in coupled mode, the atmospheric boundary condition switching algorithm is extended to accommodate ponding [*Camporese et al.*, 2010], and the feedback between overland routing and boundary condition updating allows for re-infiltration and other complex surface/subsurface interactions. The ATM + SR results in Figure 20 are therefore different from the SF and ATM curves, although the responses are nevertheless quite similar. When the kinematic celerity parameter in CATHY is set to a very high value, the fast routing triggered by this condition approaches the instantaneous removal of exfiltrating water that occurs in the ATM case. The ATM + SR* results in Figure 20 are thus closer to the SF and ATM results than the ATM+SR case was. This final series of tests has shown the algorithmic consistency between the handling of seepage face and atmospheric boundary conditions in a hydrological model. Atmospheric conditions are generally more complex however than seepage face conditions, in particular for integrated groundwater/surface water models where rainfall-infiltration-runoff partitioning is not controlled solely by subsurface flow. Even in subsurface-only mode, atmospheric boundary condition switching in a model such as CATHY also handles evaporation processes, which are usually not relevant in classic seepage flow analyses.

4. Conclusions

We have presented a modeling study of the seepage face boundary condition. The analysis is of interest for any numerical model simulating subsurface and coupled surface-subsurface processes, such as those discussed recently in *Kollet et al.* [2016]. In particular, the results apply to any model that includes representation of a seepage face boundary along a vertical downslope plane, common in hillslope and sloping aquifer studies. When, on the other hand, the seepage face intersects the land surface, the results are specifically pertinent to surface/subsurface models based on boundary condition coupling, and their broader relevance is in showing the types of interactions that any integrated model must strive to correctly resolve.

All numerical tests were performed using the CATHY model, which couples a finite element solver for the 3-D Richards equation for subsurface flow with a finite difference solver for the diffusion wave approximation of the Saint-Venant equation for overland and channel routing. A generalization of the classic algorithm for dynamic handling of seepage faces was proposed that extends easily to multiple seepage faces such as arise under conditions of heterogeneity. Four specific aspects of the seepage face boundary condition were examined: (1) the approximation errors that arise when using a simpler, static treatment of a seepage face instead of the classic dynamic approach; (2) the behavior of seepage faces under heterogeneity; (3) the interactions between a seepage face and a catchment outlet in integrated surface/subsurface modeling; and (4) the similarities and differences between seepage face and atmospheric boundary conditions in subsurface and coupled hydrological models.

In the results, we first confirmed that the generalized algorithm behaves just as the classic algorithm for homogeneous aquifers and that it handles any degree of heterogeneity unambiguously. The static (Dirichlet) condition was shown to not always be an adequate stand-in to model the dynamic seepage face boundary, and that the error committed in using static conditions increases with rainfall rate and slope angle. In the context of groundwater/surface water modeling, the scenarios addressed catchment processes involving interactions between atmospheric forcing, runoff generating mechanisms, and overland flow dynamics. We showed how seepage face and outlet boundary conditions can coexist, and we examined how they interact. In particular, rainfall partitioning between surface and subsurface flow is strongly affected by the rainfall rate and the slope angle, the first enhancing water exfiltration at the land surface and

convergent streamlines toward the outlet boundary and the second intensifying outflow from the base of the aquifer. In the final set of tests, our results showed that imposition of continuity of normal fluxes and pressure heads at the surface-subsurface interface accurately extends the seepage face algorithm to the integrated modeling framework. In particular, it was seen that seepage faces forming on the land surface are not controlled solely by subsurface flow since ponding, overland routing, and re-infiltration also impact saturation patterns and dynamics at the land surface, but the coupling algorithm based on automatic switching of atmospheric boundary conditions between Dirichlet and Neumann is able to properly resolve these surface/subsurface interactions. In the case where the model is run in subsurface-only mode, on the other hand, it was shown that the seepage face and atmospheric boundary condition algorithms are equivalent.

In a more general sense, the sequence of test cases examined in this work illustrates the complexity of flow phenomena at the atmosphere/land surface/subsurface interface. The attempt to develop generalized algorithms for the handling of boundary conditions at this interface and to show a degree of consistency between historically very different treatments applied to these conditions is important in the context of integrated hydrological modeling. Even with valid boundary condition algorithms, however, many challenges remain in accurately resolving surface/subsurface interactions. An example that involves the coexistence of catchment outlet and seepage face boundary conditions is reported in *Sulis et al*. [2011], where neglecting to represent the latter due to computational constraints (the fine grid needed to discretize stream channel geometries, including riverbanks) inevitably leads to a wet bias from overly shallow water tables that develop in response to the outlet at the land surface.

References

Beaugendre, H., A. Ern, T. Esclaffer, E. Gaume, I. Ginzburg, and C. Kao (2006), A seepage face model for the interaction of shallow water tables with the ground surface: Application of the obstacle-type method, *J. Hydrol.*, *329*(1–2), 258–273, doi:10.1016/j.jhydrol.2006.02.019.

Beven, K. (1977), Hillslope hydrographs by the finite element method, *Earth Surf. Processes Landforms*, *2*(1), 13–28, doi:10.1002/esp.3290020103.

Beven, K. (1989), Interflow, in *Unsaturated Flow in Hydrologic Modeling*, edited by H. J. Morel co-Seytoux, pp. 191–219, Springer, Netherlands, doi:10.1007/978-94-009-2352-2_7.

Beven, K., and E. F. Wood (1983), Catchment geomorphology and the dynamics of runoff contributing areas, *J. Hydrol.*, *65*(1–3), 139–158, doi:10.1016/0022-1694(83)90214-7.

Bixio, A. C., S. Orlandini, C. Paniconi, and M. Putti (1999), Coupled surface runoff and subsurface flow model for catchment simulations, in *Modelling of Transport Processes in Soils at Various Scales in Time and Space: International Workshop of the European Society of Agricultural Engineers*, pp. 583–591, Wageningen Pers, Wageningen, Netherlands.

Boughton, W. C. (1990), Systematic procedure for evaluating partial areas of watershed runoff, *J. Irrig. Drain. Eng.*, *116*(1), 83–98, doi:10.1061/(ASCE)0733-9437(1990)116:1(83).

Camporese, M., C. Paniconi, M. Putti, and S. Orlandini (2010), Surface-subsurface flow modeling with path-based runoff routing, boundary condition-based coupling, and assimilation of multisource observation data, *Water Resour. Res.*, *46*, W02512, doi:10.1029/2008WR007536.

Casagrande, A. (1937), Seepage through dams, *J. New England Water Works Assoc.*, *51*(2), 131–172.

Cloke, H. L., J.-P. Renaud, A. J. Claxton, J. J. McDonnell, M. G. Anderson, J. R. Blake, and P. D. Bates (2003), The effect of model configuration on modelled hillslope-riparian interactions, *J. Hydrol.*, *279*(1-4), 167–181, doi:10.1016/S0022-1694(03)00177-X.

Cooley, R. L. (1983), Some new procedures for numerical solution of variably saturated flow problems, *Water Resour. Res.*, *19*(5), 1271–1285, doi:10.1029/WR019i005p01271.

Coon, E. T., J. D. Moulton, and S. L. Painter (2016), Managing complexity in simulations of land surface and near-surface processes, *Environ. Modell. Softw.*, *78*, 134–149, doi:10.1016/j.envsoft.2015.12.017.

Crosta, G., and C. Prisco (1999), On slope instability induced by seepage face erosion, *Can. Geotech. J.*, *36*(6), 1056–1073, doi:10.1139/t99-062.

Delfs, J.-O., F. Blumensaat, W. Wang, P. Krebs, and O. Kolditz (2012), Coupling hydrogeological with surface runoff model in a Poltva case study in Western Ukraine, *Environ. Earth Sci.*, *65*(5), 1439–1457, doi:10.1007/s12665-011-1285-4.

Ebel, B. A., B. B. Mirus, C. S. Heppner, J. E. VanderKwaak, and K. Loague (2009), First-order exchange coefficient coupling for simulating surface water–groundwater interactions: Parameter sensitivity and consistency with a physics-based approach, *Hydrol. Processes*, *23*(13), 1949–1959, doi:10.1002/hyp.7279.

Eigenbrod, K. D., and N. R. Morgenstern (1972), A slide in cretaceous bedrock, Devon, Alberta, in *Geotechnical Practice for Stability in Open Pit Mining*, edited by C. O. Brawner and V. Milligan, pp. 223–238, Am. Inst. of Min. Eng., New York.

Ferguson, G. P., D. L. Rudolph, and J. F. Barker (2009), Hydrodynamics of a large oil sand tailings impoundment and related environmental implications, *Can. Geotech. J.*, *46*(12), 1446–1460, doi:10.1139/T09-071.

Freeze, R. A. (1971), Three-dimensional, transient, saturated-unsaturated flow in a groundwater basin, *Water Resour. Res.*, *7*(2), 347–366, doi:10.1029/WR007i002p00347.

Freeze, R. A. (1974), Streamflow generation, *Rev. Geophys.*, *12*(4), 627–647, doi:10.1029/RG012i004p00627.

Gevaert, A. I., et al. (2014), Hillslope-scale experiment demonstrates the role of convergence during two-step saturation, *Hydrol. Earth Syst. Sci.*, *18*(9), 3681–3692, doi:10.5194/hess-18-3681-2014.

Heikkinen, P. M., M. L. Räisänen, and R. H. Johnson (2009), Geochemical characterisation of seepage and drainage water quality from two sulphide mine tailings impoundments: Acid mine drainage versus neutral mine drainage, *Mine Water Environ.*, *28*(1), 30–49, doi:10.1007/s10230-008-0056-2.

Hill, A. R. (1990), Ground water flow paths in relation to nitrogen chemistry in the near-stream zone, *Hydrobiologia*, *206*(1), 39–52, doi: 10.1007/BF00018968.

Hirschfeld, R. C., and S. J. Poulos (1973), *Embankment-Dam Engineering*, Wiley, New York.

Huyakorn, P. S., E. P. Springer, V. Guvanasen, and T. Wadsworth (1986), A three-dimensional finite-element model for simulating water flow in variably saturated porous media, *Water Resour. Res.*, *22*(13), 1790–1808, doi:10.1029/WR022i013p01790.

Isaacs, L. T. (1980), Location of seepage free surface in finite element analyses, *Civil Eng. Trans., Aust.*, *22*(1), 9–16.

Keyes, D. E., et al. (2013), Multiphysics simulations challenges and opportunities, *Int. J. High Perform. Comput. Appl.*, *27*(1), 4–83, doi: 10.1177/1094342012468181.

Kolditz, O., et al. (2012), OpenGeoSys: An open-source initiative for numerical simulation of thermo-hydro-mechanical/chemical processes in porous media, *Environ. Earth Sci.*, *67*(2), 589–599, doi:10.1007/s12665-012-1546-x.

Kollet, S. J., and R. M. Maxwell (2006), Integrated surface-groundwater flow modeling; A free-surface overland flow boundary condition in a parallel groundwater flow model, *Adv. Water Resour.*, *29*(7), 945–958, doi:10.1016/j.advwatres.2005.08.006.

Kollet, S. J., and R. M. Maxwell (2008), Capturing the influence of groundwater dynamics on land surface processes using an integrated, distributed watershed model, *Water Resour. Res.*, *44*, W02402, doi:10.1029/2007WR006004.

Kollet, S. J., et al. (2016), The integrated hydrologic model intercomparison project, IH-MIP2: A second set of benchmark results to diagnose integrated hydrology and feedbacks, *Water Resour. Res.*, *53*, doi:10.1002/2016WR019191.

Lam, L., D. G. Fredlund, and S. L. Barbour (1987), Transient seepage model for saturated-unsaturated soil systems: A geotechnical engineering approach, *Can. Geotech. J.*, *24*(4), 565–580, doi:10.1139/t87-071.

Lee, Y. S., C. Y. Cheuk, and M. D. Bolton (2008), Instability caused by a seepage impediment in layered fill slopes, *Can. Geotech. J.*, *45*(10), 1410–1425, doi:10.1139/T08-067.

Liggett, J. E., A. D. Werner, and C. T. Simmons (2012), Influence of the first-order exchange coefficient on simulation of coupled surface-subsurface flow, *J. Hydrol.*, *414–415*, 503–515, doi:10.1016/j.jhydrol.2011.11.028.

Liggett, J. E., M. J. Knowling, A. D. Werner, and C. T. Simmons (2013), On the implementation of the surface conductance approach using a block-surface-subsurface hydrology model, *J. Hydrol.*, *496*, 1–8, doi:10.1016/j.jhydrol.2013.05.008.

Maxwell, R. M., et al. (2014), Surface-subsurface model intercomparison: A first set of benchmark results to diagnose integrated hydrology and feedbacks, *Water Resour. Res.*, *50*, 1531–1549, doi:10.1002/2013WR013725.

Milligan, V. (2003), Some uncertainties in embankment dam engineering, *J. Geotech. Geoenviron. Eng.*, *129*(9), 785–797, doi:10.1061/(ASCE)1090-0241(2003)129:9-(785).

Mirus, B. B., B. A. Ebel, K. Loague, and B. C. Wemple (2007), Simulated effect of a forest road on near-surface hydrologic response: Redux, *Earth Surf. Processes Landforms*, *32*(1), 126–142, doi:10.1002/esp.1387.

Neuman, S. P. (1973), Saturated-unsaturated seepage by finite elements, *J. Hydraul. Div. Am. Soc. Civ. Eng.*, *99*(HY12), 2233–2250.

Neuman, S. P., R. A. Feddes, and E. Bresler (1975), Finite element analysis of two-dimensional flow in soils considering water uptake by roots: I. Theory, *Soil Sci. Soc. Am. J.*, *39*(2), 224–230, doi:10.2136/sssaj1975.03615995003900020007x.

Niu, G.-Y., et al. (2014), Incipient subsurface heterogeneity and its effect on overland flow generation—Insight from a modeling study of the first experiment at the Biosphere 2 Landscape Evolution Observatory, *Hydrol. Earth Syst. Sci.*, *18*(5), 1873–1883, doi:10.5194/hess-18-1873-2014.

Ogden, F. L., and B. A. Watts (2000), Saturated area formation on nonconvergent hillslope topography with shallow soils: A numerical investigation, *Water Resour. Res.*, *36*(7), 1795–1804, doi:10.1029/2000WR900091.

Orlandini, S., and R. Rosso (1996), Diffusion wave modeling of distributed catchment dynamics, *J. Hydrol. Eng.*, *1*(3), 103–113, doi:10.1061/(ASCE)1084-0699(1996)1:3(103).

Orlandini, S., and R. Rosso (1998), Parametrization of stream channel geometry in the distributed modeling of catchment dynamics, *Water Resour. Res.*, *34*(8), 1971–1985, doi:10.1029/98WR00257.

Orlandini, S., G. Moretti, and J. D. Albertson (2015), Evidence of an emerging levee failure mechanism causing disastrous floods in Italy, *Water Resour. Res.*, *51*, 7995–8011, doi:10.1002/2015WR017426.

Painter, S. L., J. D. Moulton, and C. J. Wilson (2013), Modeling challenges for predicting hydrologic response to degrading permafrost, *Hydrogeol. J.*, *21*(1), 221–224, doi:10.1007/s10040-012-0917-4.

Paniconi, C., and M. Putti (1994), A comparison of Picard and Newton iteration in the numerical solution of multidimensional variably saturated flow problems, *Water Resour. Res.*, *30*(12), 3357–3374, doi:10.1029/94WR02046.

Paniconi, C., and M. Putti (2015), Physically based modeling in catchment hydrology at 50: Survey and outlook, *Water Resour. Res.*, *51*, 7090–7129, doi:10.1002/2015WR017780.

Rubin, J. (1968), Theoretical analysis of two-dimensional, transient flow of water in unsaturated and partly unsaturated soils, *Soil Sci. Soc. Am. J.*, *32*(5), 607–615, doi:10.2136/sssaj1968.03615995003200050013x.

Rulon, J. J., and R. A. Freeze (1985), Multiple seepage faces on layered slopes and their implications for slope-stability analysis, *Can. Geotech. J.*, *22*, 347–356, doi:10.1139/t85-047.

Rulon, J. J., R. Rodway, and R. A. Freeze (1985), The development of multiple seepage faces on layered slopes, *Water Resour. Res.*, *21*(11), 1625–1636, doi:10.1029/WR021i011p01625.

Shamsai, A., and T. N. Narasimhan (1991), A numerical investigation of free surface-seepage face relationship under steady state flow conditions, *Water Resour. Res.*, *27*(3), 409–421, doi:10.1029/90WR01905.

Sophocleous, M. (2002), Interactions between groundwater and surface water: The state of the science, *Hydrogeol. J.*, *10*(1), 52–67, doi:10.1007/s10040-001-0170-8.

Sterrett, R. J., and T. B. Edil (1982), Ground-water flow systems and stability of a slope, *Ground Water*, *20*(1), 5–11, doi:10.1111/j.1745-6584.1982.tb01324.x.

Sudicky, E. A., J. P. Jones, Y.-J. Park, A. E. Brookfield, and D. Colautti (2008), Simulating complex flow and transport dynamics in an integrated surface-subsurface modeling framework, *Geosci. J.*, *12*(2), 107–122, doi:10.1007/s12303-008-0013-x.

Sulis, M., S. B. Meyerhoff, C. Paniconi, R. M. Maxwell, M. Putti, and S. J. Kollet (2010), A comparison of two physics-based numerical models for simulating surface water–groundwater interactions, *Adv. Water Resour.*, *33*(4), 456–467, doi:10.1016/j.advwatres.2010.01.010.

Sulis, M., C. Paniconi, and M. Camporese (2011), Impact of grid resolution on the integrated and distributed response of a coupled surface–subsurface hydrological model for the des Anglais catchment, Quebec, *Hydrol. Processes*, *25*(12), 1853–1865, doi:10.1002/hyp.7941.

Therrien, R. E., E. A. Sudicky, and Y.-J. Park (2012), *HydroGeoSphere: A Three-Dimensional Numerical Model Describing Fully-Integrated Subsurface and Surface Flow and Transport*, User Guide, Aquanty Inc., Waterloo, Ont., Canada.

Tracy, J. C., and M. A. Mariño (1987), Seepage into variably saturated porous medium, *J. Irrig. Drain. Eng.*, *113*(2), 198–212, doi:10.1061/(ASCE)0733-9437(1987)113:2(198).

Troch, P. A., et al. (2013), The importance of hydraulic groundwater theory in catchment hydrology: The legacy of Wilfried Brutsaert and Jean-Yves Parlange, *Water Resour. Res.*, *49*, 5099–5116, doi:10.1002/wrcr.20407.

van Genuchten, M. T. (1980), A closed-form equation for predicting the hydraulic conductivity of unsaturated soils, *Soil Sci. Soc. Am. J.*, *44*(5), 892–898, doi:10.2136/sssaj1980.03615995004400050002x.

VanderKwaak, J. E. (1999), Numerical simulation of flow and chemical transport in integrated surface–subsurface hydrologic systems, PhD thesis, Univ. of Waterloo, Waterloo, Ont.

VanderKwaak, J. E., and K. Loague (2001), Hydrologic-response simulations for the R-5 catchment with a comprehensive physics-based model, *Water Resour. Res.*, *37*(4), 999–1013, doi:10.1029/2000WR900272.

Willgoose, G., and H. Perera (2001), A simple model of saturation excess runoff generation based on geomorphology, steady state soil moisture, *Water Resour. Res.*, *37*(1), 147–155, doi:10.1029/2000WR900265.